PNAS RESEARCH ARTICLE | BIOPHYSICS AND COMPUTATIONAL BIOLOGY

Integrated AlphaFold2 and DEER investigation of the conformational dynamics of a pH-dependent APC antiporter

Diego del Alamo[a,b,1], Lillian DeSousa[a], Rahul M. Nair[a], Suhaila Rahman[a], Jens Meiler[b,c], and Hassane S. Mchaourab[a,2]

Edited by Michael Grabe, University of California, San Francisco, California; received April 7, 2022; accepted July 8, 2022 by Editorial Board Member William F. DeGrado

The Amino Acid–Polyamine-Organocation (APC) transporter GadC contributes to the survival of pathogenic bacteria under extreme acid stress by exchanging extracellular glutamate for intracellular γ-aminobutyric acid (GABA). Its structure, determined in an inward-facing conformation at alkaline pH, consists of the canonical LeuT-fold with a conserved five-helix inverted repeat, thereby resembling functionally divergent transporters such as the serotonin transporter SERT and the glucose-sodium symporter SGLT1. However, despite this structural similarity, it is unclear if the conformational dynamics of antiporters such as GadC follow the blueprint of these or other LeuT-fold transporters. Here, we used double electron-electron resonance (DEER) spectroscopy to monitor the conformational dynamics of GadC in lipid bilayers in response to acidification and substrate binding. To guide experimental design and facilitate the interpretation of the DEER data, we generated an ensemble of structural models in multiple conformations using a recently introduced modification of AlphaFold2 . Our experimental results reveal acid-induced conformational changes that dislodge the Cterminus from the permeation pathway coupled with rearrangement of helices that enables isomerization between inward- and outward-facing states. The substrate glutamate, but not GABA, modulates the dynamics of an extracellular thin gate without shifting the equilibrium between inward- and outward-facing conformations. In addition to introducing an integrated methodology for probing transporter conformational dynamics, the congruence of the DEER data with patterns of structural rearrangements deduced from ensembles of AlphaFold2 models illuminates the conformational cycle of GadC underpinning transport and exposes yet another example of the divergence between the dynamics of different families in the LeuT-fold.

amino acid transport | acid resistance | membrane protein biophysics | structure prediction

Significance

The transporter GadC contributes to acid resistance in bacterial pathogens by exchanging two substrates, glutamate and γ-aminobutyric acid (GABA), using a mechanism termed alternating access. In this study, the conformational dynamics underlying alternating access were studied using a combination of spectroscopy and computational modeling. A conformationally diverse ensemble of models, generated using AlphaFold2, guided the design and interpretation of double electron-electron resonance spectroscopy experiments. We found that whereas GadC was inactive and conformationally homogeneous at neutral pH, low pH induced isomerization between two conformations. From our integrated computational/experimental investigation emerges a transport model that may be relevant to eukaryotic homologs that are involved in other cellular processes.

Found in all domains of life, transporters in the Amino Acid–Polyamine-Organocation (APC) family shuttle amino acids and their derivatives across lipid bilayers (1–5). They are presumed to mediate substrate translocation via an alternating access mechanism that entails isomerization between inward-facing (IF) and outward-facing (OF) conformations in response to substrate binding and/or release (6–8). Substrate leak across the membrane is avoided by one of two coupling mechanisms: symport, which involves cotransport of substrates and ions in the same direction followed by substrate-free isomerization, and antiport, where alternating access is strictly ligand-dependent and one substrate's import is followed by the other substrate's export (2, 4). Dysregulation and/or dysfunction of amino acid antiporters in humans has been shown to contribute to genetic diseases such as phenylketonuria, cystinuria, and lysinuric protein intolerance (9–17). Upregulation of the broad-specificity amino acid transporter LAT1 (also known as SLC7A5) and/or the cystine/glutamate exchanger xCT (SLC7A11) is a hallmark of cancer that correlates with poor prognosis and survival (15–18). LAT1 has taken further significance due to its involvement in trafficking drugs and prodrugs across the blood–brain barrier (12, 18, 19).

Although prokaryotes rely on APC transporters to acquire and retain amino acids, the most well-studied antiporters are those used by bacterial pathogens such as *Escherichia coli* O157:H7 to withstand extreme acid stress (20–25). These include the glutamate/γ-aminobutyric acid (GABA) antiporter GadC and the arginine/agmatine antiporter AdiC, which import the precursors and export the products of proton-consuming amino acid decarboxylases responsible for raising intracellular pH (21, 24, 25). AdiC adopts a homodimeric assembly, while GadC possesses a C terminus that putatively regulates pH-dependent transport (26–28) (Fig. 1*A*). Despite these unique adaptations and their functional divergence from human transporters, both exchangers have served as model systems for eukaryotic homologs since their initial structural characterization over a decade ago (29–32). The crystal structures of GadC and AdiC, which were determined

The authors declare no competing interest.

This article is a PNAS Direct Submission. M.G. is a guest editor invited by the Editorial Board.

[1]Present address: Computational Sciences, GlaxoSmithKline Research and Development, 6300 Zug, Switzerland.

[2]To whom correspondence may be addressed. Email: hassane.mchaourab@vanderbilt.edu.

This article contains supporting information online at http://www.pnas.org/lookup/suppl/doi:10.1073/pnas.2206129119/-/DCSupplemental.

Published August 15, 2022.

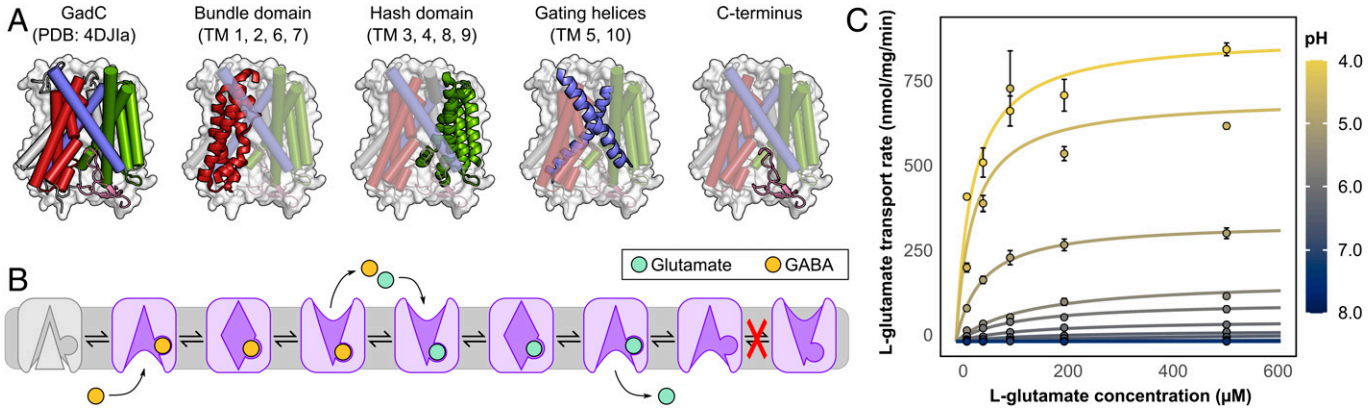

Fig. 1. Architecture and pH-dependent transport activity of GadC. (*A*) The crystal structure of GadC consists of a four-helix bundle domain, a four-helix hash domain, two gating helices, and two ancillary helices not involved in transport (not emphasized). Additionally, the C terminus is wedged into the intracellular cavity, locking the transporter into a putatively inactive conformation. (*B*) Proposed antiport mechanism consisting of inward-facing, outward-facing, and occluded conformations. This mechanism implicates glutamate and GABA in driving the outward-to-inward and inward-to-outward conformational transition, respectively, and it forbids substrate-free isomerization. (*C*) Glutamate transport by wild-type GadC reconstituted into proteoliposomes is pH dependent. Error bars correspond to the SEM ($n = 3$).

in IF and OF conformations, respectively, superimpose over recent cryo-electron microscopy (cryo-EM) structures of human orthologs and have been used, for example, for numerous drug docking studies (33–38). Nevertheless, an absence of detailed studies of their energy landscapes and conformational dynamics has hindered framing these structures in the broader context of antiport

Insights in this regard may be obtained from more distant homologs of APC transporters that have been subjects of extensive study (39–51). These include the neurotransmitter-sodium symporter SERT (52–54), the sodium-solute symporter SGLT1 (55), and bacterial model systems such as the leucine transporter LeuT (56, 57), the benzylhydantoin transporter Mhp1 (58, 59), and the betaine transporter BetP (60, 61). A large body of experimental investigation into their conformational dynamics identifies elements that are both conserved (such as substrate-dependent isomerization) and divergent (such as the effect of sodium binding on conformational dynamics) (8). However, it is unclear if patterns derived from the study of these LeuT-fold symporters extend to antiporters, particularly since the former must undergo a ligand-free isomerization step that is inhibited in the latter (6) (Fig. 1*B*).

Here, we report an investigation of the conformational dynamics of GadC using double electron-electron resonance (DEER) spectroscopy (62), a technique that has been successfully applied to the study of LeuT-fold symporters such as LeuT and Mhp1 (39–41, 63). To facilitate the interpretation of these results, we capitalized on our recent modification of the structure prediction algorithm AlphaFold2 (AF2) (64, 65) to generate structural models of GadC in multiple conformations. DEER distance distributions between spin label pairs designed based on these models suggest that the structure of GadC at acidic pH is substantially more dynamic than at neutral pH. Moreover, the C terminus, putatively responsible for regulating transport at neutral pH, detaches and becomes disordered under weakly acidic conditions. At low pH, GadC is in conformational equilibrium between inward-open and outward-open conformations, with experimental distance changes in agreement with predictions made from the AF2 models relative to the crystal structure. Substrate binding did not shift this equilibrium between conformations beyond an extracellular thin gate, a finding that contrasts with a panel of previously investigated symporters (39–41). This substrate-specific occlusion of the extracellular vestibule may be relevant to eukaryotic homologs such as xCT, which exchange amino acids in different directions with high specificity (15). Moreover, because similar elements of alternating access were observed in the sodium-hydantoin symporter Mhp1, commonalities may exist in the transport cycles of these distantly related transporters.

Results

The pH-dependent activity profile of GadC was verified by measuring radiolabeled substrate uptake into proteoliposomes. A construct of wild-type GadC cloned from *E. coli* str. O157:H7 was expressed in *E. coli* C43 (DE3), purified in β-DDM detergent micelles, and reconstituted into proteoliposomes containing 5 mM glutamate at pH 5.5 (see *Materials and Methods*). These proteoliposomes were then tested for substrate transport by detection of [^{3}H]-L-glutamate uptake as a function of both external pH and substrate concentration. Additionally, time-dependent glutamate transport was measured in proteoliposomes containing 5 mM GABA at pH 5.5 (*SI Appendix*, Fig. S1). Consistent with previous findings (26, 66), we observed a strong dependence of radioligand uptake on pH: increasing the pH from 4.0 to 6.5 reduced glutamate transport by about 97% (Fig. 1*C*).

To characterize the structural changes associated with pH-dependent activation of transport, we used site-directed spin labeling and electron paramagnetic resonance (EPR) spectroscopy (62, 67). All three endogenous cysteines in the wild-type sequence were mutated to chemically inert residues (C60V, C247A, C380V). As with previous studies on structural homologs of GadC, double-cysteine pairs were selected based on their ability to report on inter- and intradomain movements. To evaluate if these measurements were expected to fall within the detectable range for DEER measurements (15 to 60 A°) and to test whether the resulting data were consistent with the crystal structure, distance measurements were first simulated between candidate residue pairs using dummy spin labels explicitly modeled on the crystal structure (68, 69). Following purification and spin labeling, all mutants were reconstituted into proteoliposomes and tested for transport and pH-dependent inactivation at pH 5.5 (*SI Appendix*, Fig. S2) and 7.5 (*SI Appendix*, Fig. S3), respectively. Additionally, all experimental DEER measurements were carried out in nanodiscs composed of the same lipids as those of the proteoliposomes used for transport assays. This ensured that neither

the spin labels nor the membrane environment interfered with GadC's ability to traffic substrates at acidic pH or underwent substantially reduced transport at neutral pH. Finally, we note that although GadC was crystallized as an antiparallel homodimer, no experimental evidence of this quaternary assembly was detected in lipid nanodiscs.

pH-Dependent Detachment of the C Terminus Is Required for Activation. Abrogation of transport at neutral and alkaline pH has previously been attributed to the transporter's Cterminus (residues 471 to 511, shown in pink in Figs. 1*A* and 2*A*). In the crystal structure of GadC, captured at pH 8.0, the Cterminus is embedded in the intracellular cavity and obstructs both substrate passage and closure of the intracellular gate, two prerequisites of alternating access (26). To test the hypothesis that this domain detaches under acidic conditions, a double-cysteine mutant (L143C/E480C) was generated to measure the distance between spin labels in the Cterminus and in the transmembrane domain. Distance distributions of this pair reported large changes as a function of pH. At neutral pH, the average distance matched that predicted from the crystal structure, whereas a sharp increase in the magnitude, distance, and width of the distribution was observed under acidic conditions (Fig. 2*B* and *SI Appendix*, Fig. S4). A nonlinear least-squares fit to the amplitudes of the short- and long-distance components revealed that this shift occurred cooperatively with a pK_a of 6.07 ± 0.11 (Fig. 2*C*), with both short-distance components diminishing at low pH in a tightly correlated manner (*SI Appendix*, Fig. S5).

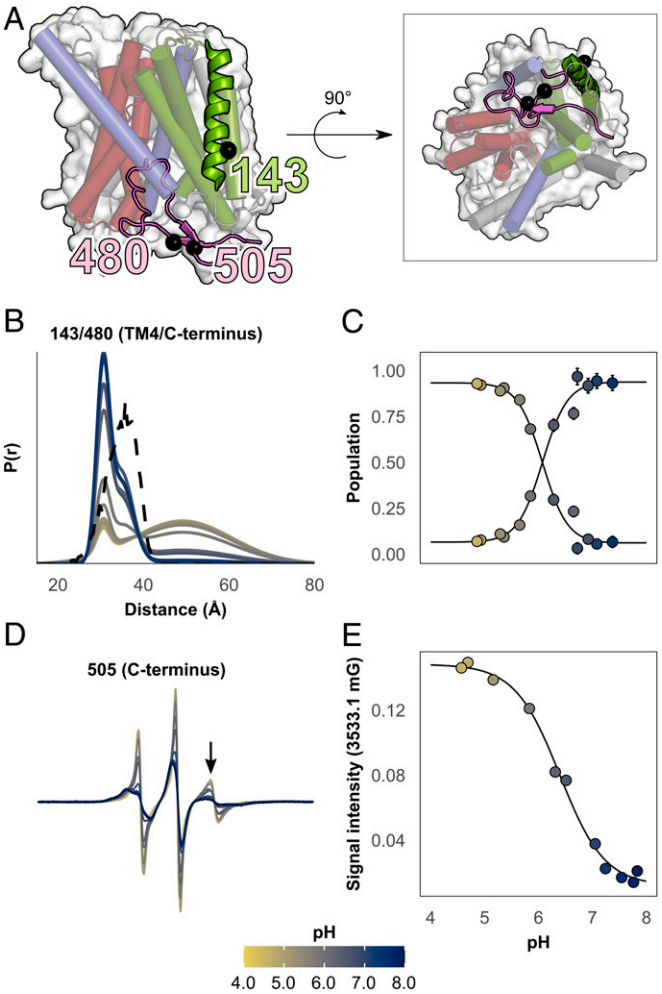

Fig. 2. Detachment of the C terminus of GadC is triggered by low pH. (*A*) Position of the C terminus, shown in pink, relative to the main transmembrane domain of the transporter. *Inset*: rotated view of the C terminus embedded in the intracellular vestibule. (*B*) Distance distributions monitoring the docking of the C terminus. At low pH, a broad long-distance component is observed in equilibrium with a distance component consistent with predictions made from the crystal structure (shown in the dashed line). (*C*) Titration measurement of the dissociation of the C terminus. Error bars correspond to 95% CIs calculated using the program GLADDvu (see *Materials and Methods*). (*D*) pH-dependent increases in conformational heterogeneity resolved by continuous-wave EPR. (*E*) Titration measurement of the mobile component of the CW spectra reveals a pH dependence similar to the distance distributions shown in *B*.

To further determine if this cooperative distance change originated from conformational disorder of the C terminus, a single-cysteine mutant was introduced (V505C). At neutral pH, the lineshape of this spin-labeled mutant's continuous wave EPR spectrum suggested that the domain was pinned to the transmembrane domain, consistent with its docked conformation in the crystal structure (Fig. 2*D*). By contrast, reducing the pH led to a sharp, highly mobile spectral component that dominated the lineshape at pH 6.0 and below, suggesting an increase in structural disorder. Nonlinear least-squares fit of the EPR spectrum high field line as a function of pH yielded a pK_a of 6.30 ± 0.04, consistent with the DEER measurements discussed above (Fig. 2 *D* and *E*). Taken together, the data corroborate the hypothesis that the C terminus detaches from the transmembrane domain under acidic conditions. Additionally, the pK_a of the C terminus undocking closely matched the pH at which transport activity is abrogated, reinforcing this domain's role in regulating substrate exchange under neutral pH conditions.

Modeling Alternative Conformations of GadC Using AF2 and Rosetta. Next, we sought to characterize the movements underpinning the transport cycle of GadC using a library of double-cysteine mutants selected to detect pH- and ligand-dependent structural changes. An OF homology model generated with RosettaCM (70), using structures of the arginine/agmatine transporter AdiC as templates (27, 28, 71, 72), initially guided experimental design but was discarded when predicted distance changes failed to correspond to experimental DEER results (*SI Appendix*, Fig. S6). We therefore used the deep learning algorithm AF2 (64) to predict the structure of GadC in multiple conformations following detachment of the C terminus by introducing several modifications described in detail in *Materials and Methods* and elsewhere (65). Model generation was followed by constrained refinement in an implicit membrane using Rosetta (73–75). To identify the breadth of the energy minimum with greater confidence, we generated 650 models and visualized the predicted conformational changes using dimensionality reduction with principal component analysis (Fig. 3).

Models generated with high confidence were distributed across three clusters, and a substantial fraction was dissimilar to the crystal structure. Visual inspection suggested that members of these three clusters could be assigned to inward-open, fully occluded, and outward-open conformations (a fourth cluster, which consisted of doubly-open models, was sparsely populated and therefore ignored during our analysis). The inward-open models differed from the crystal structure primarily in transmembrane helices (TM) 1, 6, and 7, which became slightly pinched on the intracellular side. The occluded models suggested that closure of the intracellular cavity was mediated by a large-amplitude movement of these same helices. Finally, opening of the extracellular side in the outward-open models involved translations by TM1

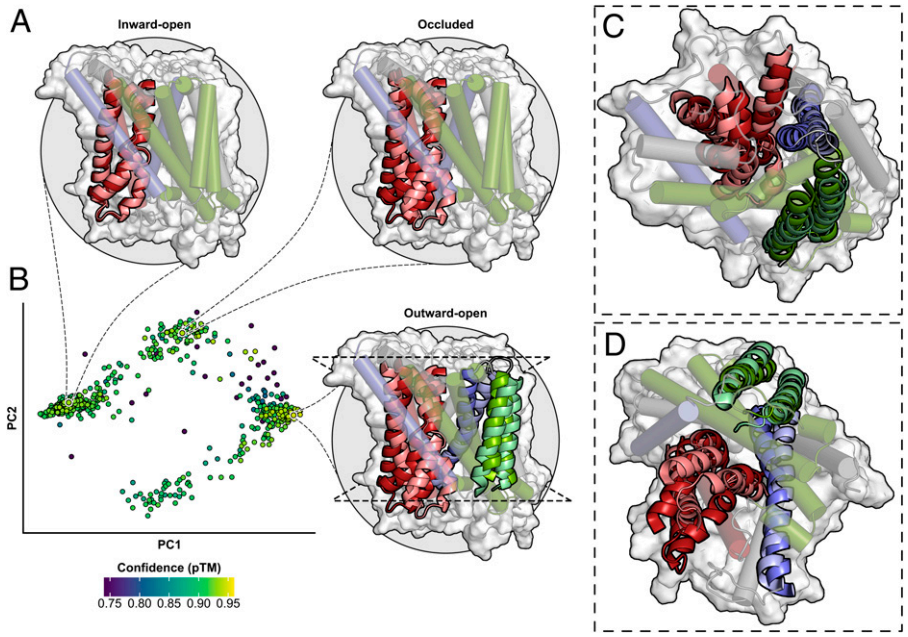

Fig. 3. Alternative conformations of GadC modeled by AF2. (*A*) Representative models generated using AF2 cluster into inward-open, fully occluded, and outward-open conformations. To highlight structural changes between the AF2 clusters and the crystal structure, key helices in each AF2 model are shown as light-colored ribbons, with the crystal structure shown in darker-colored ribbons for reference. (*B*) Dimensionality reduction using principal component analysis shows clustering of predicted conformations. Model confidence was measured using pTM, with greater values indicating greater model confidence. A fourth cluster with doubly-open models (*Bottom center*) was not analyzed. (*C* and *D*) Close-up views of the representative outward-open model from the top and bottom, respectively.

and TM6, rotation of TM4 and TM9 in the hash domain, and straightening of TM10. Overall, the proposed mechanism closely resembles that of the homolog LAT1 while deviating from that of AdiC (28, 76, 77).

A representative model from each cluster was selected based on predicted confidence values (pTM). As with the crystal structure, distance distributions between spin labels were predicted from these models for comparison with experimental DEER measurements. With these models in hand, we set out to design double-cysteine pairs to test the implied structural changes and determine the conditions under which they are sampled. For clarity, the following figures show only the OF model; predictions made from the IF and occluded models are shown in *SI Appendix*, Fig. S7.

Evaluation of the Rocking Bundle Model of Alternating Access. The extent to which the bundle domain, which comprises TMs 1, 2, 6, and 7, undergoes a rigid-body conformational change was assessed using a two-pronged approach. First, a network of double-cysteine mutants on both sides of the transporter probed the magnitude of the movements undertaken by these helices relative to reference residues located on helices not predicted to move (Figs. 4 and 5). Second, intrabundle measurements determined whether the domain itself isomerizes as a rigid body (Fig. 6). Whereas this movement was initially proposed based on comparisons of the crystal structure to outward-facing structures of AdiC (26), the ensemble of AF2 models instead predicts substantial bending and independent movement of bundle domain helices.

Distance measurements carried out at neutral pH without substrate indicated a largely homogeneous population (Figs. 4 and 5 and *SI Appendix*, Figs. S9 and S10). Unimodal peaks were observed on the intracellular side of the membrane at neutral pH, and experimental distributions closely aligned with predictions made from the crystal structure on the extracellular side.

Decreasing the pH to 4.5, which falls below the pK_a of C-terminal detachment, induced more heterogeneity on the intracellular side. Distributions between spin label pairs involving TM1 broadened and/or became multicomponent, indicating a degree of backbone flexibility absent at neutral pH. These results indicated movement of TM1 and TM6 into the intracellular cavity to partially replace the space vacated by the C terminus (Fig. 3). Additionally, lower-amplitude short-distance peaks and/or shoulders were observed in TM1/TM4, TM1/TM5, and TM4/TM6, consistent with the inward-closed AF2 models. Notable deviations between predicted and experimental distributions involving residues 15 (TM1a) and 87 (TM3) were observed, possibly due to their locations near crystal contacts (*SI Appendix*, Fig. S14).

On the extracellular side, measurements involving TM1 were also consistent with partial adoption of an outward-open conformation at low pH. Distance changes involving TM6, meanwhile, also appeared to indicate a partial population shift toward conformations similar to the outward-open models predicted by AF2. Overall, the data indicate that at low pH, the bundle-domain moves into the intracellular cavity vacated by the C-terminal domain following detachment as predicted by the inward-open AF2 model. They also suggest the concomitant sampling of a conformation consistent with the outward-open AF2 model.

A notable finding was the lack of glutamate- or GABA-dependent conformational dynamics evident in either the DEER distributions or the continuous-wave (CW) EPR spectra in the bundle domain. While very slight increases in inward- and outward-closed populations were observed, the CIs of these changes overlapped with those of GadC under apo conditions (*SI Appendix*, Figs. S9 and S10). We therefore concluded that saturating concentrations of either glutamate or GABA have no impact on the conformational equilibrium of GadC in this region at low pH. This pattern recurred throughout the structure, with one notable exception discussed below. Thus, for clarity, distributions collected with either glutamate or GABA have been omitted in the text below.

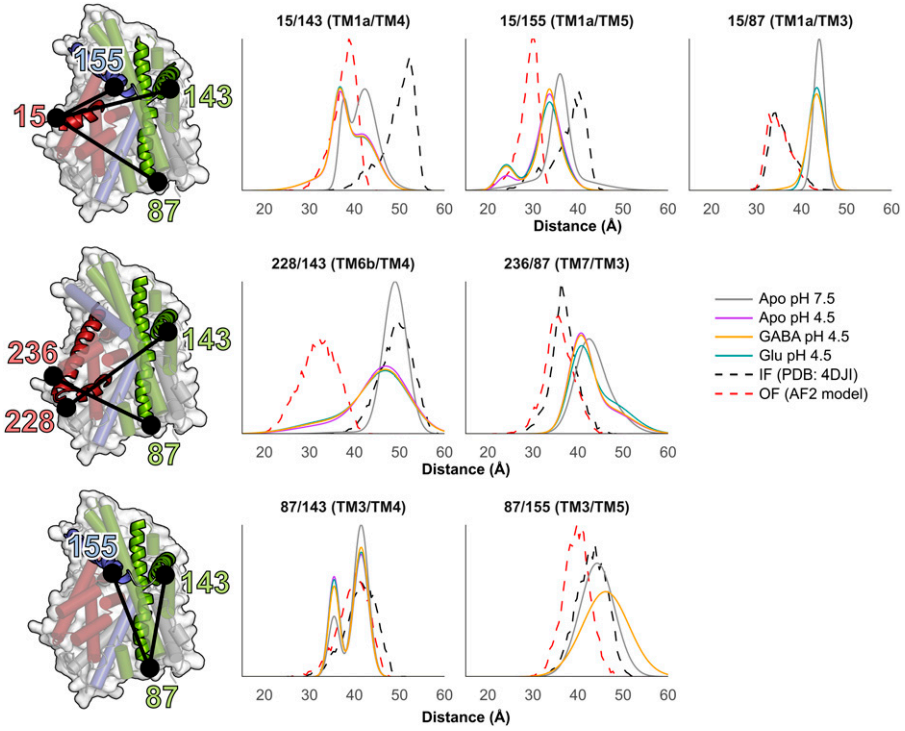

Fig. 4. Conformational changes in the bundle domain on the intracellular side. Left: cartoon depictions of GadC shown from the intracellular side. Labeled positions are indicated as black spheres in cartoons, with the bundle domain shown in red. Right: distance distributions between the bundle domain and reference sites (in blue and green) are largely unimodal at neutral pH and become more heterogeneous at low pH. Short-distance components consistent with an inward-closed model were also observed in some distributions. Substrates were not observed to affect the distance distributions. Dashed traces are predicted distributions from the structure and the outward-facing AF2 model.

The Bundle Domain Does Not Move as a Rigid Body. Comparison of the GadC crystal structure with that of the homolog AdiC prompted the hypothesis that the bundle domain facilitates alternating access by a rigid-body movement (26). In contrast, the occluded and outward-facing models generated using AF2 suggest that closure of the intracellular side is facilitated by bending of TM7 and translation of TM1 and TM6 into the space vacated by the C terminus. Both models were tested by measuring distributions within the bundle domain. However, the close distances of helices within the domain, combined with the 15-Å lower distance limit of the DEER technique, required that these measurements be carried out across the membrane (i.e., between the intracellular and extracellular sides of the transporter; Fig. 6).

Measurements between spin labels at either end of TM1 and TM6 show pH-dependent movement inconsistent with a rigid-body hypothesis. In structurally homologous LeuT-fold transporters undergoing rigid-body conformational changes, little to no movement is observed within the bundle domain (39, 78). In contrast, decreases in pH were sufficient to induce changes in both the distance distribution (Fig. 4*C*) and the CW spectra (*SI Appendix*, Fig. S11). Thus, we concluded that alternating access in GadC departs from rigid-body motions in the bundle domain as initially proposed. Instead, this conformational change appears to incorporate elements of helical translations that have been experimentally observed by crystallography and cryo-EM in closely related homologs such as LAT1 as well as more distant homologs such as LeuT and SERT (33, 52, 53, 56, 57, 77).

Lack of Large-Scale Movement in IL1 or EL4. Two additional hypotheses, implied by observations in homologous LeuT-Fold transporters, propose a role in facilitating alternating access for the amphipathic loops IL1 and EL4, which are adjacent in sequence to the bundle domain on the intracellular and extracellular sides, respectively (63, 76). In AdiC, a partially conserved tyrosine residue on IL1 has been experimentally shown to regulate pH-dependent transport (72). Its mutagenesis to alanine, but not phenylalanine, abolished transport inactivation under neutral conditions. As the corresponding residue in GadC is phenylalanine, this finding hinted at a possible role in mediating pH-dependent isomerization. Therefore, we mutated the adjacent residue, Ala77, to cysteine to both probe any pH-dependent conformational changes in this domain and to observe changes to the CW spectra indicative of environmental changes. Experimental measurements between this domain and TM3 and/or TM5 ruled out any pH-dependent helical movement (Fig. 7), while CW spectra argued against changes in the local environment of Ala77 (*SI Appendix*, Fig. S12). These results suggest that this domain is not involved in the activation mechanism of GadC and remains firmly stapled to TM3, consistent with its conservation between structures of homologous transporters (28, 76, 79).

Similarly, movement of EL4 has been shown in AdiC and other homologs such as sodium-coupled symporters including LeuT to enable access to the extracellular vestibule (28, 63, 76). However, the ensemble of AF2 models did not predict an equivalent mechanism for GadC. These distinct models were tested by labeling both ends of EL4 and measuring distances to the hash domain and to TM5. Consistent with the AF2 predictions and unlike the movements observed in other LeuT-fold homologs, we observed no evidence indicating conformational changes as a function of either pH (Fig. 7) or substrate addition (*SI Appendix*, Fig. S11) in this region. This suggests that substrate entry and exit on the extracellular side is facilitated by a different region of the transporter.

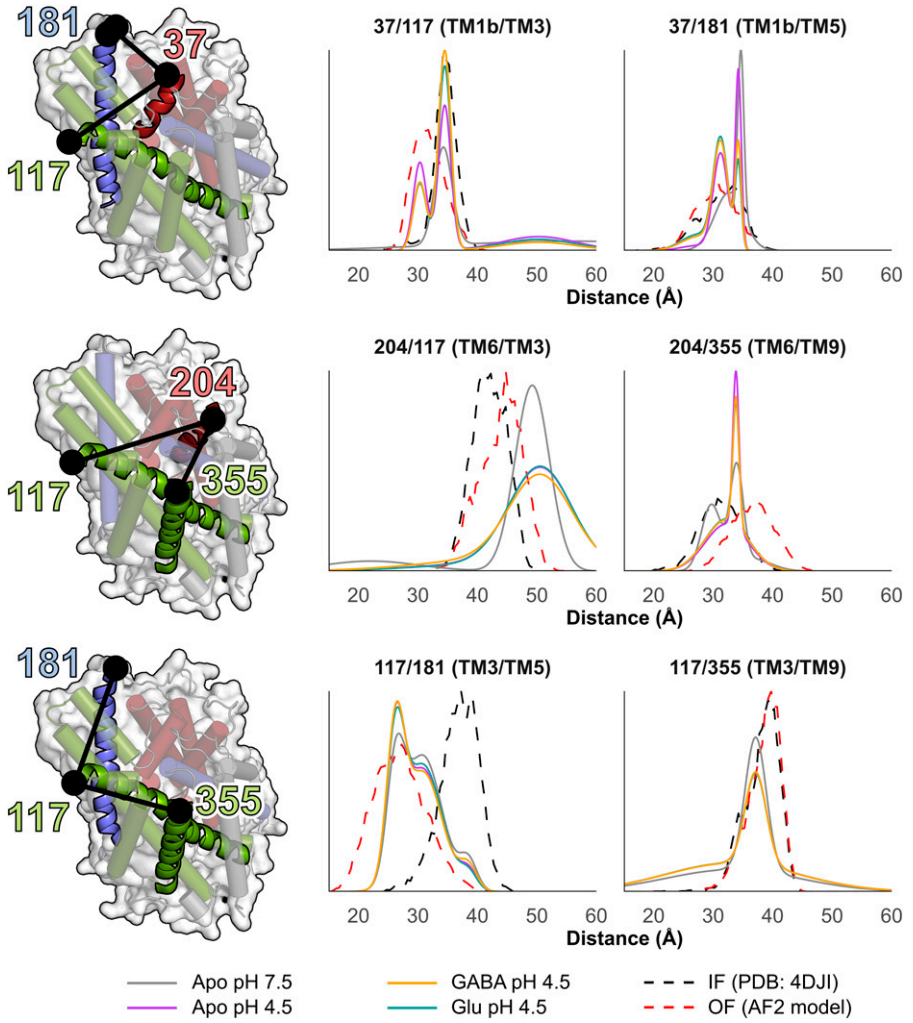

Fig. 5. Conformational changes in the bundle domain on the extracellular side. Left: cartoon depictions of GadC shown from the extracellular side, with labeled positions indicated as black spheres. Right: distance distributions overlapped with predictions made from the crystal structure at neutral pH. Low pH coincided with equilibrium shifts toward populations consistent with an outward-open model in a substrate-independent manner.

An Extracellular Thin Gate Discriminates between GABA and Glutamate. An alternative extracellular permeation pathway to that involving EL4, gleaned from the AF2 ensemble, primarily involves bending and straightening of TM10. Such a mechanism has been observed in both experimental measurements and atomistic simulations in homologous symporters such as vSGLT and Mhp1, where TM10 forms a thin gate to the substrate-binding site and undergoes movement largely uncoupled from adjacent helices (39, 41, 58, 59, 80–83). The AF2 ensemble, by contrast, predicted that this helix's position is tightly coupled to that of TM9 in the hash domain.

Distance measurements from this helix at neutral pH were defined by a single sharp component, which corroborated observations made throughout the structure (Fig. 8 *A* and *B*). Decreasing the pH led to a bimodal distribution with peaks spaced 10 Å apart, consistent with predictions made from comparison of the crystal structure and the OF AF2 model. Notably, whereas this distribution was unchanged following addition of saturating concentrations of GABA, glutamate appeared to promote closure of this thin gate, a finding that was corroborated across multiple biological repeats (*SI Appendix*, Fig. S13). No such effect was observed in measurements involving the extracellular side of TM9, which is linked to TM10 by a triple-glycine motif. Thus, these data demonstrate that the dynamics of these two helices are uncoupled in the OF state. Moreover, they indicate a mechanism by which GadC differentiates between its two substrates that may be relevant to homologous APC transporters.

Discussion

In this report, we investigated the structure and conformational dynamics of the pH-dependent glutamate/GABA antiporter GadC, a member of the APC family and a homolog of human transporters implicated in various diseases, by integrating DEER spectroscopy with high-confidence structure prediction using AF2. This methodology capitalizes on a recent modification of AF2 by our group to model GadC in multiple distinct conformations (65). Although models generated using the unmodified version of AF2 and our modified implementation have been reported to closely align with experimental high-resolution structures, these models do not account for factors known to induce structural changes, such as pH and substrate, as well as the effect of the lipid bilayer. Moreover, the sampling frequency of distinct structural clusters has been shown to correlate poorly with experimentally measured conformational dynamics (84–86). Thus, the integrated methodology showcased here uses the ensemble of structural models to guide the design of high-information content DEER experiments, thereby increasing the throughput of spectroscopic and biochemical investigations. Experimental distance

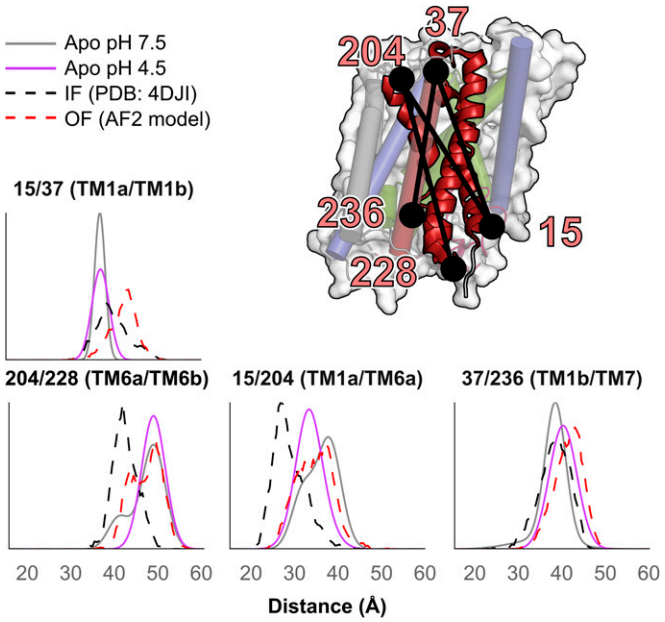

Fig. 6. The bundle domain of GadC does not behave as a rigid body. Measurements between spin labels (indicated by black spheres) across the membrane indicate a degree of intra- and interhelical flexibility. Low-pH measurements with GABA and glutamate overlapped with apo low-pH measurements and are omitted for clarity.

distributions are then compared to predictions made from both the crystal structure and representative AF2 models. Unlike integrative modeling pipelines that use the data as modeling restraints (87–90), our approach was reinforced by the correspondence between DEER distributions predicted by the AF2 models and the experimentally resolved distance components.

Our study assessed how GadC's conformational cycle underpins coupled glutamate import and GABA export, whereas isomerization of the substrate-free transporter is inhibited. GadC is both functionally coupled to and cotranscribed with the soluble enzyme GadB, which irreversibly decarboxylates glutamate into GABA (91). In some species of bacteria, the intracellular concentration of GABA has been shown to reach up to 80 mM during acid stress, almost certainly exceeding that of the extracellular milieu by several orders of magnitude (92). The differences between the concentrations of glutamate on either side of the membrane may not be as extreme (93, 94). Thus, we propose that the export step likely drives the conformational cycle of GadC.

This functional context is the foundation for one of this study's key conclusions, that is, the absence of detectable substrate-induced conformational changes throughout most of the structure of GadC. By contrast, pH changes shifted the equilibrium between IF and OF conformations, particularly on the intracellular side and the C terminus. Indeed, substrate-induced movements were limited to the extracellular half of TM10, which was predicted by our ensemble of AF2 models to bend and straighten in the outward-closed and outward-open conformations, respectively. Glutamate, but not GABA, pushed the conformational equilibrium toward the former relative to apo conditions. However, the remainder of the structure appeared insensitive to the addition of either substrate. Thus, we propose that substrates principally modulate the height of the energy barrier separating these two states, rather than the energetics difference between GadC conformations (Fig. 8*C*).

Remarkably, the proposed conformational cycle deviates from those of structurally homologous sodium-coupled symporters, which have been shown to undergo substantial rearrangements in response to substrate binding (39–41, 47). However, our results may indicate that the contribution of substrates to the conformational equilibrium of GadC closely parallels the role played by the driving sodium ion in Mhp1 and vSGLT, as saturating concentrations had no effect on the equilibrium between OF and IF of either symporter relative to ligand-free conditions (39, 41, 47). Instead, as was demonstrated using cysteine accessibility measurements, hydrogen-deuterium exchange/mass spectrometry, and EPR spectroscopy, sodium binding introduced an impassable kinetic barrier preventing uncoupled sodium flux down its concentration gradient (39, 47, 95, 96). We propose that glutamate and GABA play the inverse role in GadC: Their binding reduces the kinetic barrier separating the IF and OF conformations while minimally affecting the energetics of the underlying equilibrium. Similarly, their release into the cytoplasmic or periplasmic space introduces a large energy barrier to substrate-free isomerization. We note that while the DEER data do not reflect changes in kinetic

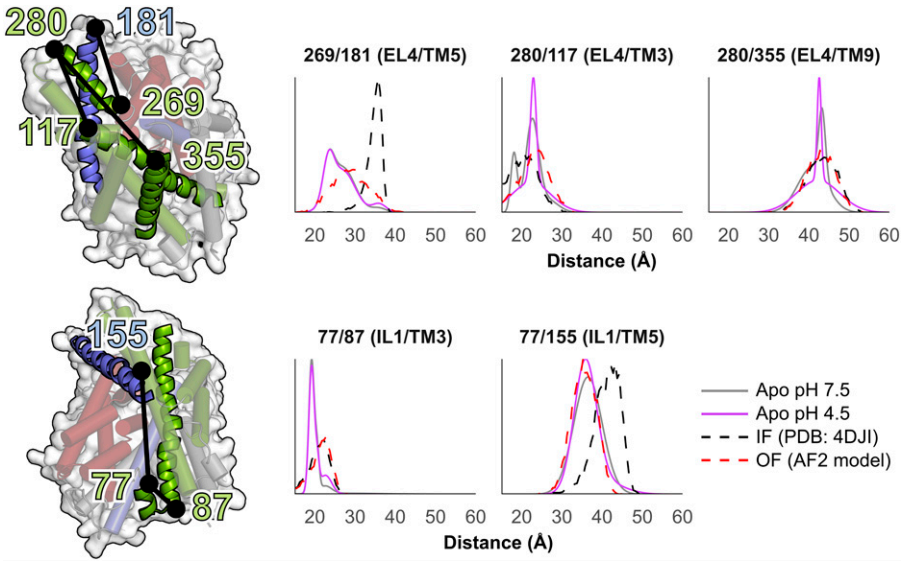

Fig. 7. No large-scale pH-dependent changes in the positions of IL1 and EL4. *Top*: Position of EL4 as measured from residues 269 and 280. *Bottom*: IL1. Cartoon depictions of GadC shown on the left along with positions of labeling sites indicated by black spheres.

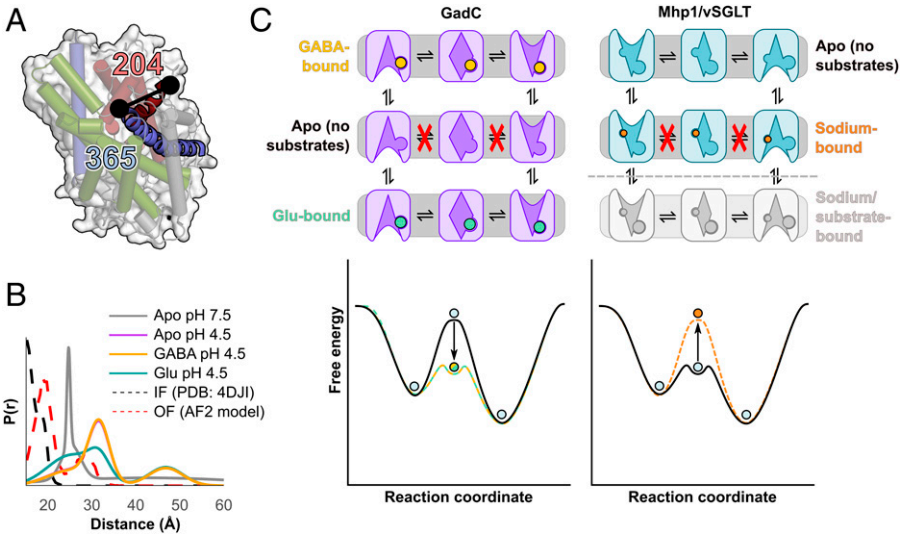

Fig. 8. TM10 undergoes substrate-dependent dynamics independent from the hash domain. (*A*) Cartoon depiction of GadC highlighting TMs 6a and 10 and the spin-labeling sites (black spheres). (*B*) Distance distributions between TM6a and TM10 (residues 204/365) demonstrate that glutamate, but not GABA (purple and yellow traces are superimposable), induces a shift in the population of distance components (the long-distance peak at 48 Å is likely an aggregation artifact also present in the apo pH 7.5 trace). (*C*) Proposed activation and glutamate-GABA antiport mechanism (*Left*). The C-terminus detaches at weakly acidic pH, allowing isomerization to proceed. Glutamate and GABA lower an energy barrier separating the inward- and outward-facing conformations. No large-scale substrate-dependent conformational changes were observed in GadC that were equivalent to binding of sodium and substrates to sodium-coupled symporters such as Mhp1 and vSGLT (shown on the *Right*). The greyed-out portion of the transport cycle of Mhp1 and vSGLT showing sodium/substrate symport is not directly translatable to our proposed mechanism of antiport.

barrier, this proposal is consistent with previous results for the homologous serine-threonine antiporter SteT showing that ligand binding reduced a kinetic energy barrier during unfolding (97).

A feature of our proposed conformational cycle is that the dynamics of TM10 selectively responds to glutamate but not GABA binding. Intriguingly, although AF2 predicted that this helix acts as an extracellular thin gate, our ensemble of models suggested that its motion was tightly coupled to that of TM9. In contrast, the DEER data reveal that TM10, but not TM9, distinguishes between glutamate and GABA binding. This was particularly striking given the observed correspondence between distance changes predicted by AF2 and distance changes observed by DEER (*SI Appendix*, Fig. S13). Further, the dynamics observed in TM10 closely mirrors the dynamics of its pseudosymmetric counterpart TM5 in poly-specific amino acid symporters, such as LeuT, the bending of which correlates with overall transport rate (98, 99). As GadC is highly specific for glutamate and GABA, it was not possible to establish an equivalent trend between transport rate and bending in TM10. Nevertheless, this observation may be relevant to homologs such as LAT1, a broad-specificity amino acid exchanger that was proposed to undergo a similar mechanism of alternating access defined by movement in the bundle domain, TM4, TM9, and TM10 (33, 77). However, whereas the outward-facing cryo-EM structures of LAT1, bound to competitive inhibitors, were exclusively determined in detergent micelles, the AF2 models of GadC were experimentally corroborated under more physiologically relevant conditions. Thus, whether the dynamics of TM10 are broadly equivalent to those of TM5 in sodium-coupled amino acid symporters remains to be determined.

Our work presented here establishes an experimental methodology for investigation of conformational changes underpinning transport. The ensembles of AF2 models, validated by DEER distance measurements, will allow further computational analysis such as molecular dynamics simulations, as well as more detailed testing of transport mechanisms via site-directed mutants to trap specific conformations, as has been shown for other transporters (100).

Materials and Methods

Site-Directed Mutagenesis. A codon-optimized version of the GadC gene from *E. coli* str. O157:H7 (Genscript) was cloned into a pET19b vector encoding an N-terminal deca-histidine tag. A cysteine-less construct (C60V, C246A, C380V) was generated from this template using site-directed mutagenesis (QuikChange). All single- and double-cysteine mutants were similarly generated from this cysteine-free construct and verified by Sanger sequencing using both T7 forward and reverse primers.

Expression, Purification, and Spin Labeling of GadC. Plasmids encoding either wild-type or mutant GadC were transformed into competent *E. coli* str. C43 (DE3) cells and overexpressed in 1 L minimal media A supplemented with ampicillin (Gold Biotechnology) as previously described. Upon reaching an absorbance (optical density, 600 nm) of 0.7 to 0.8, GadC expression was induced by adding 1 mM isopropyl β-d-1-thiogalactopyranoside (Gold Biotechnology), and the temperature was dropped to 20 °C. Cells were harvested after 16 h by centrifugation at 5,500 *g* for 15 min, resuspended in 22 mL lysis buffer (100 mM KPi, 10 mM dithiothreitol [DTT], pH 7.5), and lysed by sonication. After centrifugation at 9,000 *g* for 15 min, the supernatant was collected and ultracentrifuged at 200,000 *g* for 90 min.

The pelleted membrane fractions were then solubilized in resuspension buffer (50 mM Tris/Mes, 200 mM NaCl, 20% glycerol, and 1 mM DTT, pH 7.5) containing 1% β-DDM (Anatrace) and stirred on ice for 60 min. Insoluble material was removed by ultracentrifugation at 200,000 *g* for 30 min, and the supernatant was incubated with 1.0 mL Ni-NTA Superflow (Qiagen) resin at 4 °C for 2 h with 25 mM imidazole. After washing with 10 column volumes of resuspension buffer containing 50 mM imidazole and 0.05% β-DDM, purified GadC was eluted from the resin using resuspension buffer with 250 mM imidazole and 0.05% β-DDM.

Following the addition of 60 mM Mes, single- and double-cysteine mutants were labeled with three rounds of 20-fold molar excess MTSSL (Enzo Life Sciences) per cysteine at room temperature and moved to ice overnight after 4 h. Samples were then concentrated using Amicon Ultra 50,000 Dalton molecular weight cutoff (MWCO) filter concentrators (Millipore) to a final concentration no greater than 3 mg/mL, as reported by absorbance at 280 nm (ε = 67,840 M^{-1} cm^{-1}), and purified into 200 mM Tris/Mes, pH 7.2, 20% glycerol, and 0.05% β-DDM by size exclusion chromatography using a Shodex KW-803 column with guard column. Peak fractions were eluted at 9.5 to 10.5 mL and were isolated for further studies.

Reconstitution of GadC into Proteoliposomes. A 3:1 ratio (wt/wt) of *E. coli* polar lipids and L-α-phosphocholine (Avanti Polar Lipids) was dissolved in

chloroform and evaporated with a rotary evaporator. After overnight desiccation in a vacuum chamber, lipids were resuspended in the appropriate buffer, homogenized by 10 cycles of freeze-thawing, and stored in small aliquots at −80 °C.

Lipids prepared for liposomes were resuspended in 25 mM KPi, 150 mM KCl, pH 5.5, and either 5 mM L-glutamate or 5 mM GABA to a final concentration of 20 mg/mL (16.4 mM). Before reconstitution, lipids were diluted and destabilized with the addition of 1.25% octyl-β-D-glucopyranoside (Anatrace) and extruded through a 400-nm membrane filter (Whatman). Purified GadC was added to the sample at a 1:200 ratio (wt/wt), bringing the final lipid concentration to 5 mg/mL. Following a 30-min incubation at room temperature, detergent was removed from the sample by the gradual addition of 400 mg/mL SM-2 polystyrene Bio-Beads (Bio-Rad) over the course of 4 h. After rocking overnight in the dark, the proteoliposome solution was cleared of biobeads and ultracentrifuged at 150,000 *g* for 60 min. Proteoliposomes were then resuspended in external buffer (25 mM KPi, 150 mM KCl, pH 5.5) and ultracentrifuged to remove external substrates. After this ultracentrifugation step was repeated a total of three times, proteoliposomes were suspended in external buffer at a final lipid concentration of 100 mg/mL. GadC concentration was then quantified using sodium dodecyl sulfate polyacrylamide gel electrophoresis and densitometry (ImageJ v. 1.53), with purified GadC in β-DDM serving as a standard curve.

Transport Assays. In vitro transport assays were carried out either in triplicate (concentration dependent, Fig. 1 and *SI Appendix*, Figs. S2 and S3) or in duplicate (time dependent, *SI Appendix*, Fig. S1) as previously described (26). An additional baseline measurement was performed on ice. Glutamic acid (between 25 μM and 1 mM) was added to external buffer and checked for pH immediately prior to all transport experiments. For the time-dependent transport glutamate/GABA exchange assay shown in *SI Appendix*, Fig. S1, a fixed external glutamate concentration of 50 μM at pH 5.5 was used. In both experiments, proteoliposomes (2 μL) were added to external buffer (98 μL) containing 1 μCi [^{3}H]-L-glutamic acid (∼200 nM) and gently agitated. For titration experiments on wild-type GadC, proteoliposomes (1 μL) were added to external buffer (99 μL) containing 1 μCi [^{3}H]-L-glutamic acid. Substrate uptake proceeded for 2 min at 25 °C and was quenched by adding ice-cold stop buffer (25 mM glycine, 150 mM KCl, pH 9.5) and vacuum-filtering the solution through a 0.22-μm GSTF filter (Millipore) presoaked in stop buffer. The filter was then washed with an additional 6 mL stop buffer, removed, and added to 5 mL Ecoscint H scintillation solution (National Diagnostics). Following quantitation, data were analyzed using Michaelis-Menten kinetics using the *curve_fit* function implemented in SciPy (101). Baseline measurements were subtracted from the 25 °C measurements.

Reconstitution of GadC into Lipid Nanodiscs. Lipids for nanodisc reconstitution were prepared as described above and resuspended in 50 mM Tris/Mes, pH 7.5, to a final concentration of 20 mM. MSP1D1E3 was purified as previously described (102). Nanodisc reconstitution proceeded using a molar ratio of 1:8 GadC:MSP1D1E3, 1:50 MSP1D1E3:lipid, and 1:5 lipid:cholate. Detergents were gradually removed from the solution using SM-2 Bio-Beads as previously described (102). After overnight incubation, biobeads were removed from the solution using a 0.20-μm filter. Nanodisc-reconstituted GadC was then isolated from empty nanodiscs by size-exclusion chromatography using a Superdex 200 Increase 10/300 GL column into 50 mM Tris/Mes, pH 7.5, 10% glycerol and was concentrated using an Amicon Ultra 100,000 Dalton MWCO filter concentrator (Millipore). The pH of all protein samples was carefully determined using a microelectrode and adjusted using 1 M citrate and 1 M Tris. Protein concentration was then evaluated using CW-EPR spectroscopy as previously described (103). Glycerol was added to all DEER samples to a final concentration of 23% vol/vol, and the samples were then flash-frozen in liquid nitrogen prior to DEER spectroscopy.

CW-EPR and DEER Spectroscopy and Data Analysis. Spin-labeled GadC was characterized using CW-EPR at 25 °C using a Bruker EMX spectrometer operating at a frequency of 9.5 GHz, a 10-mW incident power, and a modulation amplitude of 1.6 G. DEER measurements were carried out on an Elexsys E580 EPR spectrometer using a dead-time–free four-pulse protocol (104) at either 50 K (for 143C/480C) or 83 K (all other double-cysteine mutants). Sample volumes ranged from 10 to 50 μL. Pulse lengths were as follows: 10 ns to 14 ns (first π/2 pulse), 20 ns (second and fourth π pulse), and 40 ns (third π pulse). The pump and observation frequencies were separated by 62.26 MHz. Echo decay data were analyzed into distance distributions using GLADDvu with the last 500 ns of the signal truncated (105, 106). Model parameters, which included the number of total Gaussian distributions, means and widths of distributions across different conditions, and the background signal, were chosen by minimizing the Bayesian Information Criterion (106, 107).

To analyze the pH titration distance data collected using GadC 143C/480C, the long-distance component was isolated from the two short-distance components and was fitted with a sigmoid function using the *curve_fit* function as implemented in SciPy (101). For all DEER pairs, the distance distributions were compared to predictions generated by the Molecular Dynamics of Dummy Spin Labels program , which was accessed using the CHARMM-GUI web server (69).

Generation of Structural Models in Multiple Conformations Using AF2 and Rosetta. The structure of GadC was modeled using AlphaFold v.2.0.1 using a modified version of ColabFold (64, 108). Multiple sequence alignments were generated using MMSeqs2 (109). Several modifications were introduced to the default pipeline to obtain alternative conformations of GadC (65). First, all inward-open structures were removed from the list of templates fetched by MMSeqs2 prior to modeling, leaving inward-facing occluded structures of ApcT (79) (Protein Data Bank [PDB] 3GIAa and 3GI9c) and GkPApcT (110) (PDB 5OQTa and 6F34a), as well as outward-facing structures of AdiC (71, 72) (PDB 3OB6b and 5J4Ib) and LAT1 (33, 77) (PDB 7DSQb). To ensure that all templates were used, the sequence identity cutoff for inclusion was lowered from 10 to 1%. Second, the configuration *subsample_templates*, which is set to *False* by default, was set to *True*. Third, the depth of the multiple sequence alignment (MSA, set by *max_msa_clusters*) was reduced to between 8 and 20 sequences, and the total number of sequences provided to the protocol (*max_extra_msa*) was set to double that number. Finally, refinement by OpenMM was replaced by Cartesian minimization using Rosetta FastRelax (75). For this step, the *membrane_high-res_Menv_smooth* scoring function was used, with the score terms *coordinate_-constraint* set to 1.0, *cart_bonded* set to 0.5, and *pro_close* set to 0.0 (74). The membrane bilayer's position was calculated using OCTOPUS as previously described (111). The Cartesian coordinates of all backbone heavy atoms were constrained to their initial positions by weights inversely proportional to their predicted local distance difference test [pLDDT; (112)] values:

$$E = \sum_{i=1} \left(\frac{d_i}{1.5 * exp(4 * (0.7 - pLDDT_i))} \right)^2 \quad [1]$$

Here, d_i is the *i*th atom's distance from its initially predicted position, and *E* refers to the coordinate constraint energy term (113) (we note that the pLDDT values provided by AF2 ranged from 0 to 100 and were therefore divided by 100 prior to calculating these values). The side chain heavy atoms of residues with pLDDT values exceeding 0.9 were similarly constrained in Cartesian space. This pipeline was used to generate 650 structural models of GadC without its C terminus (residues 471 to 511), with 25 models generated for each MSA depth by each of the two *monomer_ptm* neural networks capable of using templates. These models were then aligned to the crystal structure using TM-Align (114, 115) and projected onto a lower-dimensional space using principal component analysis as implemented by SciKit-Learn (116). Only the positions of alpha carbons belonging to helical residues were considered, and atoms belonging to loop residues were omitted from this analysis.

Data, Materials, and Software Availability. All study data are included in the article and/or *SI Appendix*. Plasmids are available from the corresponding author upon request.

ACKNOWLEDGMENTS. This study was funded by the NIH (Grant No. GM 128087). We thank Dr. Derek P. Claxton for critical review of this manuscript, Dr. Richard Stein and Dr. Eric J. Hustedt for fruitful discussions regarding the interpretation of DEER confidence bands, and Dr. Smriti Mishra for helpful guidance on nanodisc reconstitution.

Author affiliations: [a]Department of Molecular Physiology and Biophysics, Vanderbilt University, Nashville, TN 37212; [b]Department of Chemistry, Vanderbilt University, Nashville, TN 37212; and [c]Institute for Drug Discovery, Leipzig University, Leipzig, Germany 04109

Author contributions: D.d.A, S.R., J.M., and H.S.M. designed research; D.d.A., L.D., R.M.N., and S.R. performed research; D.d.A., L.D., R.M.N., and S.R. analyzed data; D.d.A. and H.S.M. wrote the paper; and J.M. and H.S.M. provided funding and resources for the study.

1. Å. Västermark, M. H. Saier Jr., Evolutionary relationship between 5 + 5 and 7 + 7 inverted repeat folds within the amino acid-polyamine-organocation superfamily. *Proteins* **82**, 336–346 (2014).
2. P. Kandasamy, G. Gyim-esi, Y. Kanai, M. A. Hediger, Amino acid transporters revisited: New views in health and disease. *Trends Biochem. Sci.* **43**, 752–789 (2018).
3. D. Fotiadis, Y. Kanai, M. Palacín, The SLC3 and SLC7 families of amino acid transporters. *Mol. Aspects Med.* **34**, 139–158 (2013).
4. A. Nicolàs-Aragó, J. Fort, M. Palacín, E. Errasti-Murugarren, Rush hour of LATs towards their transport cycle. *Membranes (Basel)* **11**, 602 (2021).
5. D. L. Jack, I. T. Paulsen, M. H. Saier, The amino acid/polyamine/organocation (APC) superfamily of transporters specific for amino acids, polyamines and organocations. *Microbiology (Reading)* **146**, 1797–1814 (2000).
6. L. R. Forrest, G. Rudnick, The rocking bundle: A mechanism for ion-coupled solute flux by symmetrical transporters. *Physiology (Bethesda)* **24**, 377–386 (2009).
7. D. Drew, O. Boudker, Shared molecular mechanisms of membrane transporters. *Annu. Rev. Biochem.* **85**, 543–572 (2016).
8. K. Kazmier, D. P. Claxton, H. S. Mchaourab, Alternating access mechanisms of LeuT-fold transporters: Trailblazing towards the promised energy landscapes. *Curr. Opin. Struct. Biol.* **45**, 100–108 (2017).
9. M. J. Calonge *et al.*, Cystinuria caused by mutations in *rBAT*, a gene involved in the transport of cystine. *Nat. Genet.* **6**, 420–425 (1994).
10. E. B. Knöpfel *et al.*, Dysfunctional LAT2 amino acid transporter is associated with cataract in mouse and humans. *Front. Physiol.* **10**, 688 (2019).
11. H. Sason *et al.*, Asc-1 transporter regulation of synaptic activity via the tonic release of D-serine in the forebrain. *Cereb. Cortex* **27**, 1573–1587 (2017).
12. D. C. Tărlungeanu *et al.*, Impaired amino acid transport at the blood brain barrier is a cause of autism spectrum disorder. *Cell* **167**, 1481–1494.e18 (2016).
13. L. Feliubadaló *et al.*; International Cystinuria Consortium, Non-type I cystinuria caused by mutations in SLC7A9, encoding a subunit (bo,+AT) of rBAT. *Nat. Genet.* **23**, 52–57 (1999).
14. D. Torrents *et al.*, Identification of SLC7A7, encoding y+LAT-1, as the lysinuric protein intolerance gene. *Nat. Genet.* **21**, 293–296 (1999).
15. M. Lo, V. Ling, Y. Z. Wang, P. W. Gout, The x_c^- cystine/glutamate antiporter: A mediator of pancreatic cancer growth with a role in drug resistance. *Br. J. Cancer* **99**, 464–472 (2008).
16. X. Fan *et al.*, Impact of system L amino acid transporter 1 (LAT1) on proliferation of human ovarian cancer cells: A possible target for combination therapy with anti-proliferative aminopeptidase inhibitors. *Biochem. Pharmacol.* **80**, 811–818 (2010).
17. A. K. Najumudeen *et al.*; CRUK Rosetta Grand Challenge Consortium, The amino acid transporter SLC7A5 is required for efficient growth of KRAS-mutant colorectal cancer. *Nat. Genet.* **53**, 16–26 (2021).
18. Y. Kanai, Amino acid transporter LAT1 (SLC7A5) as a molecular target for cancer diagnosis and therapeutics. *Pharmacol. Ther.* **230**, 107964 (2022).
19. J. Rautio, M. Gynther, K. Laine, LAT1-mediated prodrug uptake: A way to breach the blood-brain barrier? *Ther. Deliv.* **4**, 281–284 (2013).
20. J. W. Foster, *Escherichia coli* acid resistance: Tales of an amateur acidophile. *Nat. Rev. Microbiol.* **2**, 898–907 (2004).
21. E. M. Krammer, M. Prévost, Function and regulation of acid resistance antiporters. *J. Membr. Biol.* **252**, 465–481 (2019).
22. U. Kanjee, W. A. Houry, Mechanisms of acid resistance in *Escherichia coli*. *Annu. Rev. Microbiol.* **67**, 65–81 (2013).
23. B. M. Hersh, F. T. Farooq, D. N. Barstad, D. L. Blankenhorn, J. L. Slonczewski, A glutamate-dependent acid resistance gene in *Escherichia coli*. *J. Bacteriol.* **178**, 3978–3981 (1996).
24. G. w. Park, F. Diez-Gonzalez, A novel glutamate-dependent acid resistance among strains belonging to the *Proteeae* tribe of *Enterobacteriaceae*. *FEMS Microbiol. Lett.* **237**, 303–309 (2004).
25. H. Richard, J. W. Foster, *Escherichia coli* glutamate- and arginine-dependent acid resistance systems increase internal pH and reverse transmembrane potential. *J. Bacteriol.* **186**, 6032–6041 (2004).
26. D. Ma *et al.*, Structure and mechanism of a glutamate-GABA antiporter. *Nature* **483**, 632–636 (2012).
27. Y. Fang *et al.*, Structure of a prokaryotic virtual proton pump at 3.2 A resolution. *Nature* **460**, 1040–1043 (2009).
28. X. Gao *et al.*, Structure and mechanism of an amino acid antiporter. *Science* **324**, 1565–1568 (2009).
29. L. Napolitano *et al.*, Novel insights into the transport mechanism of the human amino acid transporter LAT1 (SLC7A5). Probing critical residues for substrate translocation. *Biochim. Biophys. Acta Gen. Subj.* **1861**, 727–736 (2017).
30. H. Ylikangas *et al.*, Quantitative insight into the design of compounds recognized by the L-type amino acid transporter 1 (LAT1). *ChemMedChem* **9**, 2699–2707 (2014).
31. E. G. Geier *et al.*, Structure-based ligand discovery for the Large-neutral Amino Acid Transporter 1, LAT-1. *Proc. Natl. Acad. Sci. U.S.A.* **110**, 5480–5485 (2013).
32. A. Rosell *et al.*, Structural bases for the interaction and stabilization of the human amino acid transporter LAT2 with its ancillary protein 4F2hc. *Proc. Natl. Acad. Sci. U.S.A.* **111**, 2966–2971 (2014).
33. R. Yan, X. Zhao, J. Lei, Q. Zhou, Structure of the human LAT1-4F2hc heteromeric amino acid transporter complex. *Nature* **568**, 127–130 (2019).
34. Y. Lee *et al.*, Cryo-EM structure of the human L-type amino acid transporter 1 in complex with glycoprotein CD98hc. *Nat. Struct. Mol. Biol.* **26**, 510–517 (2019).
35. J. L. Parker *et al.*, Molecular basis for redox control by the human cystine/glutamate antiporter system xc. *Nat. Commun.* **12**, 7147 (2021).
36. R. Yan *et al.*, Cryo-EM structure of the human heteromeric amino acid transporter $b^{0,+}$AT-rBAT. *Sci. Adv.* **6**, eaay6379 (2020).
37. R. Yan, J. Zhou, Y. Li, J. Lei, Q. Zhou, Structural insight into the substrate recognition and transport mechanism of the human LAT2-4F2hc complex. *Cell Discov.* **6**, 82 (2020).
38. C. F. Rodriguez *et al.*, Structural basis for substrate specificity of heteromeric transporters of neutral amino acids. *Proc. Natl. Acad. Sci. U.S.A.* **118**, e2113573118 (2021).
39. K. Kazmier, S. Sharma, S. M. Islam, B. Roux, H. S. Mchaourab, Conformational cycle and ion-coupling mechanism of the Na^+/hydantoin transporter Mhp1. *Proc. Natl. Acad. Sci. U.S.A.* **111**, 14752–14757 (2014).
40. K. Kazmier *et al.*, Conformational dynamics of ligand-dependent alternating access in LeuT. *Nat. Struct. Mol. Biol.* **21**, 472–479 (2014).
41. A. Paz *et al.*, Conformational transitions of the sodium-dependent sugar transporter, vSGLT. *Proc. Natl. Acad. Sci. U.S.A.* **115**, E2742–E2751 (2018).
42. I. R. Möller *et al.*, Probing the conformational impact of detergents on the integral membrane protein LeuT by global HDX-MS. *J. Proteomics* **225**, 103845 (2020).
43. P. S. Merkle *et al.*, Substrate-modulated unwinding of transmembrane helices in the NSS transporter LeuT. *Sci. Adv.* **4**, eaar6179 (2018).
44. S. Adhikary *et al.*, Conformational dynamics of a neurotransmitter:sodium symporter in a lipid bilayer. *Proc. Natl. Acad. Sci. U.S.A.* **114**, E1786–E1795 (2017).
45. I. R. Möller *et al.*, Conformational dynamics of the human serotonin transporter during substrate and drug binding. *Nat. Commun.* **10**, 1687 (2019).
46. A. K. Nielsen *et al.*, Substrate-induced conformational dynamics of the dopamine transporter. *Nat. Commun.* **10**, 2714 (2019).
47. A. N. Calabrese *et al.*, Topological dissection of the membrane transport protein Mhp1 derived from cysteine accessibility and mass spectrometry. *Anal. Chem.* **89**, 8844–8852 (2017).
48. G. Jeschke, C. Wegener, M. Nietschke, H. Jung, H. J. Steinhoff, Interresidual distance determination by four-pulse double electron-electron resonance in an integral membrane protein: The Na^+/proline transporter PutP of *Escherichia coli*. *Biophys. J.* **86**, 2551–2557 (2004).
49. M. Sala-Rabanal *et al.*, Bridging the gap between structure and kinetics of human SGLT1. *Am. J. Physiol. Cell Physiol.* **302**, C1293–C1305 (2012).
50. D. D. F. Loo, B. A. Hirayama, M. H. Karakossian, A. K. Meinild, E. M. Wright, Conformational dynamics of hSGLT1 during Na^+/glucose cotransport. *J. Gen. Physiol.* **128**, 701–720 (2006).
51. D. D. F. Loo *et al.*, Conformational changes couple Na^+ and glucose transport. *Proc. Natl. Acad. Sci. U.S.A.* **95**, 7789–7794 (1998).
52. J. A. Coleman, E. M. Green, E. Gouaux, X-ray structures and mechanism of the human serotonin transporter. *Nature* **532**, 334–339 (2016).
53. J. A. Coleman *et al.*, Serotonin transporter-ibogaine complexes illuminate mechanisms of inhibition and transport. *Nature* **569**, 141–145 (2019).
54. D. Yang, E. Gouaux, Illumination of serotonin transporter mechanism and role of the allosteric site. *Sci. Adv.* **7**, eabl3857 (2021).
55. L. Han *et al.*, Structure and mechanism of the SGLT family of glucose transporters. *Nature* **601**, 274–279 (2022).
56. A. Yamashita, S. K. Singh, T. Kawate, Y. Jin, E. Gouaux, Crystal structure of a bacterial homologue of Na^+/Cl^--dependent neurotransmitter transporters. *Nature* **437**, 215–223 (2005).
57. H. Krishnamurthy, E. Gouaux, X-ray structures of LeuT in substrate-free outward-open and apo inward-open states. *Nature* **481**, 469–474 (2012).
58. S. Weyand *et al.*, Structure and molecular mechanism of a nucleobase-cation-symport-1 family transporter. *Science* **322**, 709–713 (2008).
59. T. Shimamura *et al.*, Molecular basis of alternating access membrane transport by the sodium-hydantoin transporter Mhp1. *Science* **328**, 470–473 (2010).
60. S. Ressl, A. C. Terwisscha van Scheltinga, C. Vonrhein, V. Ott, C. Ziegler, Molecular basis of transport and regulation in the Na^+/betaine symporter BetP. *Nature* **458**, 47–52 (2009).
61. C. Perez, C. Koshy, O. Yildiz, C. Ziegler, Alternating-access mechanism in conformationally asymmetric trimers of the betaine transporter BetP. *Nature* **490**, 126–130 (2012).
62. G. Jeschke, DEER distance measurements on proteins. *Annu. Rev. Phys. Chem.* **63**, 419–446 (2012).
63. D. P. Claxton *et al.*, Ion/substrate-dependent conformational dynamics of a bacterial homolog of neurotransmitter:sodium symporters. *Nat. Struct. Mol. Biol.* **17**, 822–829 (2010).
64. J. Jumper *et al.*, Highly accurate protein structure prediction with AlphaFold. *Nature* **596**, 583–589 (2021).
65. D. Del Alamo, D. Sala, H. S. Mchaourab, J. Meiler, Sampling alternative conformational states of transporters and receptors with AlphaFold2. *eLife* **11**, e75751 (2022).
66. D. Ma, P. Lu, Y. Shi, Substrate selectivity of the acid-activated glutamate/γ-aminobutyric acid (GABA) antiporter GadC from *Escherichia coli*. *J. Biol. Chem.* **288**, 15148–15153 (2013).
67. H. S. McHaourab, P. R. Steed, K. Kazmier, Toward the fourth dimension of membrane protein structure: Insight into dynamics from spin-labeling EPR spectroscopy. *Structure* **19**, 1549–1561 (2011).
68. S. M. Islam, R. A. Stein, H. S. McHaourab, B. Roux, Structural refinement from restrained-ensemble simulations based on EPR/DEER data: Application to T4 lysozyme. *J. Phys. Chem. B* **117**, 4740–4754 (2013).
69. S. Jo *et al.*, CHARMM-GUI PDB manipulator for advanced modeling and simulations of proteins containing nonstandard residues. *Adv. Protein Chem. Struct. Biol.* **96**, 235–265 (2014).
70. Y. Song *et al.*, High-resolution comparative modeling with RosettaCM. *Structure* **21**, 1735–1742 (2013).
71. H. Ilgü *et al.*, Insights into the molecular basis for substrate binding and specificity of the wild-type L-arginine/agmatine antiporter AdiC. *Proc. Natl. Acad. Sci. U.S.A.* **113**, 10358–10363 (2016).
72. S. Wang, R. Yan, X. Zhang, Q. Chu, Y. Shi, Molecular mechanism of pH-dependent substrate transport by an arginine-agmatine antiporter. *Proc. Natl. Acad. Sci. U.S.A.* **111**, 12734–12739 (2014).
73. J. K. Leman *et al.*, Macromolecular modeling and design in Rosetta: Recent methods and frameworks. *Nat. Methods* **17**, 665–680 (2020).
74. V. Yarov-Yarovoy, J. Schonbrun, D. Baker, Multipass membrane protein structure prediction using Rosetta. *Proteins* **62**, 1010–1025 (2006).
75. P. Conway, M. D. Tyka, F. DiMaio, D. E. Konerding, D. Baker, Relaxation of backbone bond geometry improves protein energy landscape modeling. *Protein Sci.* **23**, 47–55 (2014).
76. X. Gao *et al.*, Mechanism of substrate recognition and transport by an amino acid antiporter. *Nature* **463**, 828–832 (2010).
77. R. Yan *et al.*, Mechanism of substrate transport and inhibition of the human LAT1-4F2hc amino acid transporter. *Cell Discov.* **7**, 16 (2021).
78. S. Weyand *et al.*, The alternating access mechanism of transport as observed in the sodium-hydantoin transporter Mhp1. *J. Synchrotron Radiat.* **18**, 20–23 (2011).
79. P. L. Shaffer, A. Goehring, A. Shankaranarayanan, E. Gouaux, Structure and mechanism of a Na+-independent amino acid transporter. *Science* **325**, 1010–1014 (2009).
80. S. Faham *et al.*, The crystal structure of a sodium galactose transporter reveals mechanistic insights into Na+/sugar symport. *Science* **321**, 810–814 (2008).

81. A. Watanabe *et al.*, The mechanism of sodium and substrate release from the binding pocket of vSGLT. *Nature* **468**, 988–991 (2010).
82. K. J. Simmons *et al.*, Molecular mechanism of ligand recognition by membrane transport protein, Mhp1. *EMBO J.* **33**, 1831–1844 (2014).
83. J. L. Adelman *et al.*, Simulations of the alternating access mechanism of the sodium symporter Mhp1. *Biophys. J.* **101**, 2399–2407 (2011).
84. B. P. Vani, A. Aranganathan, D. Wang, P. Tiwary, From sequence to Boltzmann weighted ensemble of structures with AlphaFold2-RAVE. biorXiv [Preprint Accessed 1 June 2022] (2022). doi.org/10.1101/2022.05.25.493365.
85. J. Jumper *et al.*, Applying and improving AlphaFold at CASP14. *Proteins* **89**, 1711–1721 (2021).
86. D. Del Alamo, C. Govaerts, H. S. Mchaourab, AlphaFold2 predicts the inward-facing conformation of the multidrug transporter LmrP. *Proteins* **89**, 1226–1228 (2021).
87. D. Del Alamo *et al.*, Rapid simulation of unprocessed DEER decay data for protein fold prediction. *Biophys. J.* **118**, 366–375 (2020).
88. M. H. Tessmer *et al.*, Characterization of the ExoU activation mechanism using EPR and integrative modeling. *Sci. Rep.* **10**, 19700 (2020).
89. D. Del Alamo, K. L. Jagessar, J. Meiler, H. S. Mchaourab, Methodology for rigorous modeling of protein conformational changes by Rosetta using DEER distance restraints. *PLoS Comput. Biol.* **17**, e1009107 (2021).
90. O. Duss *et al.*, Structural basis of the non-coding RNA RsmZ acting as a protein sponge. *Nature* **509**, 588–592 (2014).
91. G. Capitani *et al.*, Crystal structure and functional analysis of *Escherichia coli* glutamate decarboxylase. *EMBO J.* **22**, 4027–4037 (2003).
92. K. A. G. Karatzas, O. Brennan, S. Heavin, J. Morrissey, C. P. O'Byrne, Intracellular accumulation of high levels of γ-aminobutyrate by *Listeria monocytogenes* 10403S in response to low pH: Uncoupling of γ-aminobutyrate synthesis from efflux in a chemically defined medium. *Appl. Environ. Microbiol.* **76**, 3529–3537 (2010).
93. P. Kirchhoff *et al.*, An amino acid transporter involved in gastric acid secretion. *Pflugers Arch.* **451**, 738–748 (2006).
94. Y. Nagata *et al.*, High concentrations of D-amino acids in human gastric juice. *Amino Acids* **32**, 137–140 (2007).
95. J. Fan *et al.*, Crystal structures of LeuT reveal conformational dynamics in the outward-facing states. *J. Biol. Chem.* **296**, 100609 (2021).
96. Y. W. Zhang *et al.*, Structural elements required for coupling ion and substrate transport in the neurotransmitter transporter homolog LeuT. *Proc. Natl. Acad. Sci. U.S.A.* **115**, E8854–E8862 (2018).
97. C. A. Bippes *et al.*, Substrate binding tunes conformational flexibility and kinetic stability of an amino acid antiporter. *J. Biol. Chem.* **284**, 18651–18663 (2009).
98. D. Calugareanu, I. R. Möller, S. G. Schmidt, C. J. Loland, K. D. Rand, Probing the impact of temperature and substrates on the conformational dynamics of the neurotransmitter:sodium symporter LeuT: Impact on LeuT of temperature and Ala/Leu binding. *J. Mol. Biol.* **434**, 167356 (2022).
99. J. Grouleff, S. Søndergaard, H. Koldsø, B. Schiøtt, Properties of an inward-facing state of LeuT: Conformational stability and substrate release. *Biophys. J.* **108**, 1390–1399 (2015).
100. A. T. Bozzi *et al.*, Structures in multiple conformations reveal distinct transition metal and proton pathways in an Nramp transporter. *eLife* **8**, 1–63 (2019).
101. P. Virtanen *et al.*; SciPy 1.0 Contributors, SciPy 1.0: Fundamental algorithms for scientific computing in Python. *Nat. Methods* **17**, 261–272 (2020).
102. K. L. Jagessar, D. P. Claxton, R. A. Stein, H. S. Mchaourab, Sequence and structural determinants of ligand-dependent alternating access of a MATE transporter. *Proc. Natl. Acad. Sci. U.S.A.* **117**, 4732–4740 (2020).
103. P. Zou, H. S. McHaourab, Increased sensitivity and extended range of distance measurements in spin-labeled membrane proteins: Q-band double electron-electron resonance and nanoscale bilayers. *Biophys. J.* **98**, L18–L20 (2010).
104. M. Pannier, S. Veit, A. Godt, G. Jeschke, H. W. Spiess, Dead-time free measurement of dipole-dipole interactions between electron spins. *J. Magn. Reson.* **142**, 331–340 (2000).
105. E. J. Hustedt, R. A. Stein, H. S. Mchaourab, Protein functional dynamics from the rigorous global analysis of DEER data: Conditions, components, and conformations. *J. Gen. Physiol.* **153**, e201711954 (2021).
106. E. J. Hustedt, F. Marinelli, R. A. Stein, J. D. Faraldo-Gómez, H. S. Mchaourab, Confidence analysis of DEER data and its structural interpretation with ensemble-biased metadynamics. *Biophys. J.* **115**, 1200–1216 (2018).
107. O. Schiemann *et al.*, Benchmark test and guidelines for DEER/PELDOR experiments on nitroxide-labeled biomolecules. *J. Am. Chem. Soc.* **143**, 17875–17890 (2021).
108. M. Mirdita *et al.*, ColabFold: Making protein folding accessible to all. *Nat. Methods* **19**, 679–682 (2022).
109. M. Steinegger, J. Söding, MMseqs2 enables sensitive protein sequence searching for the analysis of massive data sets. *Nat. Biotechnol.* **35**, 1026–1028 (2017).
110. K. E. J. Jungnickel, J. L. Parker, S. Newstead, Structural basis for amino acid transport by the CAT family of SLC7 transporters. *Nat. Commun.* **9**, 550 (2018).
111. H. Viklund, A. Elofsson, OCTOPUS: Improving topology prediction by two-track ANN-based preference scores and an extended topological grammar. *Bioinformatics* **24**, 1662–1668 (2008).
112. V. Mariani, M. Biasini, A. Barbato, T. Schwede, lDDT: A local superposition-free score for comparing protein structures and models using distance difference tests. *Bioinformatics* **29**, 2722–2728 (2013).
113. N. Hiranuma *et al.*, Improved protein structure refinement guided by deep learning based accuracy estimation. *Nat. Commun.* **12**, 1340 (2021).
114. Y. Zhang, J. Skolnick, TM-align: A protein structure alignment algorithm based on the TM-score. *Nucleic Acids Res.* **33**, 2302–2309 (2005).
115. Y. Zhang, J. Skolnick, Scoring function for automated assessment of protein structure template quality. *Proteins* **57**, 702–710 (2004).
116. F. Pedregosa *et al.*, Scikit-learn: Machine learning in Python. *J. Mach. Learn. Res.* **12**, 2825–2830 (2011).